PNAS RESEARCH ARTICLE | EARTH, ATMOSPHERIC, AND PLANETARY SCIENCES

Modes of Pangean lake level cyclicity driven by astronomical climate pacing modulated by continental position and pCO_2

Jan Landwehrs[a,b,1], Georg Feulner[b], Matteo Willeit[b], Stefan Petri[b], Benjamin Sames[a], Michael Wagreich[a], Jessica H. Whiteside[c,d], and Paul E. Olsen[e]

Edited by Isabel Montanez, University of California, Davis, CA; received March 11, 2022; accepted September 20, 2022

Orbital cyclicity is a fundamental pacemaker of Earth's climate system. The Newark–Hartford Basin (NHB) lake sediment record of eastern North America contains compelling geologic expressions of this cyclicity, reflecting variations of climatic conditions in tropical Pangea during the Late Triassic and earliest Jurassic (∼233 to 199 Ma). Climate modeling enables a deeper mechanistic understanding of Earth system modulation during this unique greenhouse and supercontinent period. We link major features of the NHB record to the combined climatic effects of orbital forcing, paleogeographic changes, and atmospheric pCO_2 variations. An ensemble of transient, orbitally driven climate simulations is assessed for nine time slices, three atmospheric pCO_2 values, and two paleogeographic reconstructions. Climatic transitions from tropical humid to more seasonal and ultimately semiarid are associated with tectonic drift of the NHB from ∼5 °N to 20 °N. The modeled orbital modulation of the precipitation–evaporation balance is most pronounced during the 220 to 200 Ma interval, whereas it is limited by weak seasonality and increasing aridity before and after this interval. Lower pCO_2 at around 205 Ma contributes to drier climates and could have led to the observed damping of sediment cyclicity. Eccentricity-modulated precession dominates the orbitally driven climate response in the NHB region. High obliquity further amplifies summer precipitation through the seasonal shifts in the tropical rainfall belt. Regions with other proxy records are also assessed, providing guidance toward an integrated picture of global astronomical climate forcing in the Late Triassic and ultimately of other periods in Earth history.

Triassic | Jurassic | Newark Basin | orbital cycles | climate model

Significance

The glacial cycles of the last 3 My demonstrate the fundamental control of astronomical variations on Earth's climate system. Sedimentary records of orbital climate cycles from much further in Earth's past provide insights into its behavior under different conditions and potentially the factors leading into and out of extreme climatic states. We use climate model simulations to identify drivers of climatic changes recorded in lake sediments of the Newark–Hartford Basins of the eastern United States. During their formation from 233 to 199 Ma, these were located in the tropics of the supercontinent Pangea. We show how the combination of astronomical forcing and the plate tectonic drift as well as fluctuating atmospheric pCO_2 could have caused the reconstructed cycles and trends.

Cyclic variations in Earth's orbit and axial orientation cause changes in insolation and consequently in climate (e.g., refs. 1–4). Understanding this omnipresent astronomical forcing on different Earth system states (e.g., the greenhouse world of the last supercontinent Pangea and the icehouse world of the Pleistocene) provides fundamental insights into Earth's climate dynamics throughout its past and potentially into its future. Lake sediments from the Newark and Hartford Basins (eastern North America) compose one of the most compelling records of astronomically driven climate cyclicity on ancient Earth (5, 6). These sediments accumulated over a period of more than 30 My from the Late Triassic into the Early Jurassic (233 to 199 Ma) in rift basins that formed during the initial breakup of Pangea (5, 7). The largely lacustrine deposits display pronounced cyclicities, interpreted as periodic variations of lake water depth linked to orbitally driven changes in the climatic precipitation–evaporation balance (5, 8). Based on cores from the Newark Basin Coring Project and Army Corps of Engineers (9), augmented with cores from the Hartford Basin, the composite sequence is one of the longest continuous lacustrine records available (6, 7, 10) and provides a reference for early Mesozoic orbital climate pacing in the tropics (11). Cyclicities have been quantitatively assessed from facies-based depth ranks and sediment color as proxies of lake water depth and thus climate (5, 7, 8, 11). A hierarchy of sedimentary successions clusters into groups expressing the ∼20-ky climatic precession cycle (the 1- to 25-m-thick Van Houten cycles, depending on basin position and age), modulated by ∼100 and 405 ky eccentricity cycles (5, 7, 8).

Building on these efforts, further clarification of the effects of different orbital parameters on a world characterized by a single supercontinent and a greenhouse climate—and the expression of these effects at specific proxy localities—yields a more consistent picture of astronomical pacing of Earth's climate system. The present study contributes to this by providing a comprehensive climate model framework for the interpretation of the Newark–Hartford composite record. To identify Late Triassic climate trends and cycles and their drivers, we analyze an ensemble of orbitally forced global climate simulations, which reflects paleogeographic changes as well as a range of cooler and warmer climate states related to atmospheric pCO_2 values. Orbital effects during some Mesozoic or earlier time periods have been studied with climate models before, using sets of fixed orbital parameters

Author contributions: J.L., G.F., M. Willeit, M. Wagreich, J.H.W., and P.E.O. designed research; J.L. performed research; M. Willeit contributed new analytic tools; J.L. analyzed data; and J.L., G.F., M. Willeit, S.P., B.S., M. Wagreich, J.H.W., and P.E.O. wrote the paper.

The authors declare no competing interest.

This article is a PNAS Direct Submission.

[1]To whom correspondence may be addressed. Email: jan.landwehrs@posteo.de.

This article contains supporting information online at https://www.pnas.org/lookup/suppl/doi:10.1073/pnas.2203818119/-/DCSupplemental.

Published November 7, 2022.

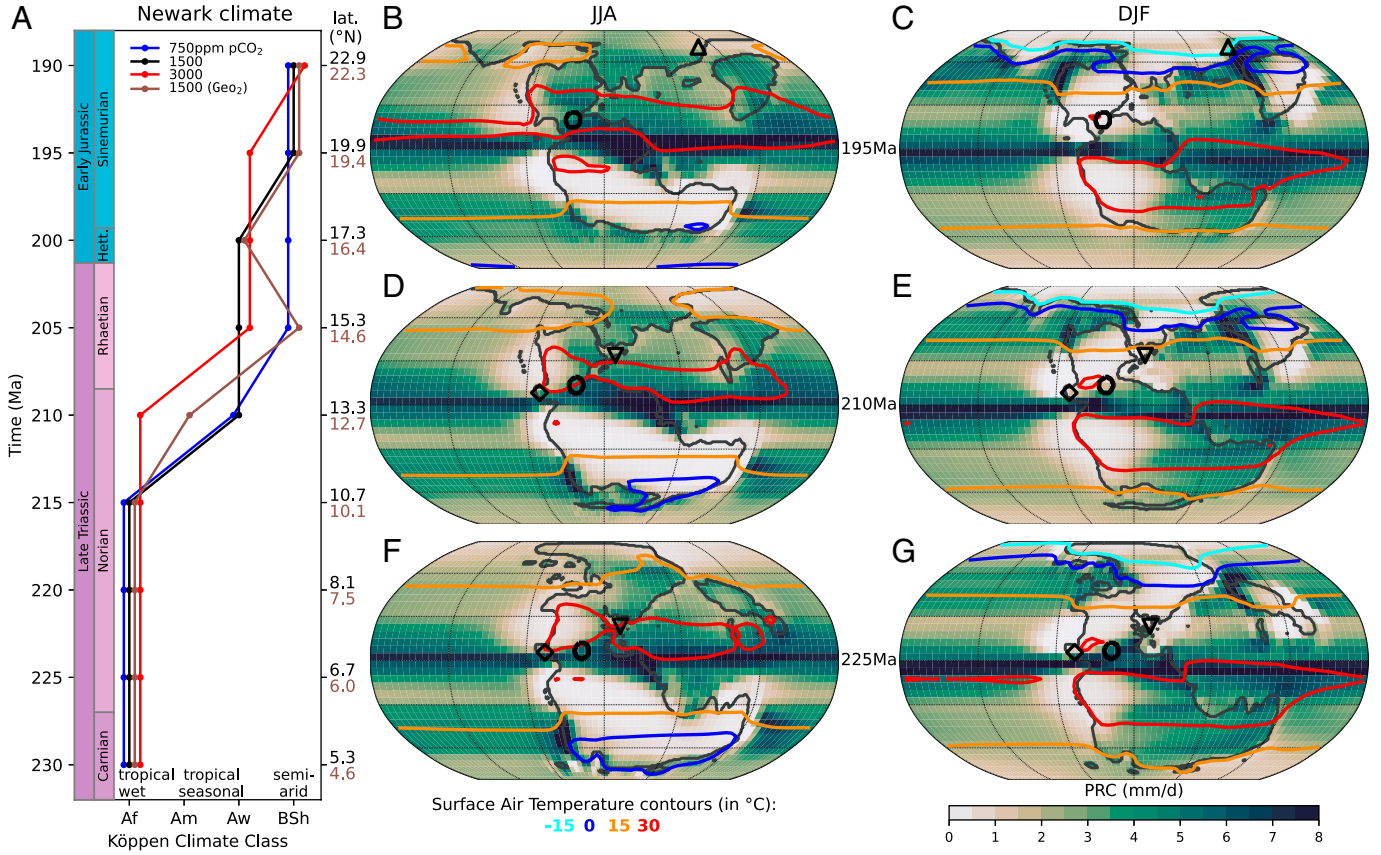

Fig. 1. Long-term average climate conditions (*A*) in the NHB area and (*B–G*) on the globe through the Late Triassic and earliest Jurassic. (*A*) Köppen climate classes determined from the simulated long-term average monthly temperatures and precipitation rates in the NHB area marked by the black circle in the maps (*B–G*). Axis labels on the right side indicate the latitude of the NHB from the two paleogeographic reconstructions at the respective time slice [black, $\mathtt{Geo}_1$ (20); brown, $\mathtt{Geo}_2$ (21, 22); *Materials and Methods*]. (*B–G*) Seasonal precipitation rates (colors) and surface air temperatures (colored contours for 30, 15, 0, and −15 °C) for boreal summer (June, July, and August [JJA]; *Left*) and winter (December, January, and February [DJF]; *Right*). Shown are long-term averages from three selected simulations for 225, 210, and 205 Ma at $pCO_2 = 1{,}500$ ppm, using the $\mathtt{Geo}_1$ paleogeographies. Coastlines are shown by black contours. Locations of the NHB (circles), Germanic Basin (downward triangles), Junggar Basin (upward triangles), and Colorado Plateau (diamonds) are indicated.

(e.g., refs. 12–18). Here we assess climate responses in the Newark–Hartford Basins (NHB) to both astronomical and plate tectonic dynamics through transient climate simulations on orbital time scales for a number of Late Triassic time slices. Because this approach is global in nature, we also use it to link contemporaneous records from different localities to form a more integrated picture of climate trends and cycles across Pangea in the Late Triassic.

Humid–Seasonal–Dry Climate Transition due to Continental Drift

We employ the Earth System Model called CLIMBER-X (19), especially its coupled atmosphere, ocean, sea ice, and land surface models, all discretized on a $5° \times 5°$ horizontal grid. Transient simulations are run for 250 ky with paleogeographies for nine Late Triassic to Early Jurassic time slices (230 to 190 Ma in 5-My steps) at three atmospheric pCO_2 values (750, 1,500, and 3,000 ppm). All simulations are exposed to an idealized orbital forcing that cyclically modulates eccentricity e, precession angle ω, and obliquity ε with periods of 100, 40, and 20 ky, respectively (*Materials and Methods*).

Before analyzing dynamical orbital effects, we characterize the modeled general climatic setting of the NHB area and effects of continental drift and pCO_2 across the considered time slices. For this, averages over the last 200 ky of each simulation are considered. The NHB was initially located within the tropical rainfall belt that broadened toward the warm Tethys Sea in the east that acted as a source of moisture, in contrast to the drier western Pangea (Fig. 1 *F* and *G*). At these low latitudes (~4–10 °N), the area experienced warm and humid conditions with weak seasonality that correspond to *Af* climates in the Köppen classification of modern climate zones (Fig. 1*A*; based on simulated monthly temperatures and precipitation rates) (23). This is true from 230 to 215 Ma independent of pCO_2 and the two considered paleogeographic reconstructions ($\mathtt{Geo}_1$ and $\mathtt{Geo}_2$; *Materials and Methods*). Around these modeled long-term average conditions (*Materials and Methods*), orbital climate modulation and other variability can lead to dry or wet extreme periods, as discussed in following sections. With Pangea's northward drift, the NHB moved to higher latitudes, and seasonal contrasts increase with higher summer temperatures (T) and precipitation rates (PRC) and cooler, drier winters (Fig. 1 *B–E*). This is also expressed as a transition to monsoonal (*Am*) and savanna (*Aw*) climates with pronounced wet and dry seasons (210 to 195 Ma, at ~10 to 20 °N) and finally to semiarid steppe climates (*BSh*) with very hot summers and less rainfall when the NHB reached subtropical latitudes (195 to 190 Ma, ~20 to 23 °N). The simulated wind and moisture transport to the NHB are generally dominated by northeasterly trade winds during winter and southeasterly winds during summer which supported diminishing rainfall as the region drifted to the subtropics (*SI Appendix*, section 7 and Figs. S26–S28).

In absolute terms, the simulated regional annual mean T^{ann}_{NHB} at 230 Ma ranges from 24 to 31 °C (at $pCO_2 = 750$ and 3,000 ppm) and increases continuously by 5 to 6 °C until 190 Ma, while PRC^{ann}_{NHB} reaches a peak of 5 to 6.6 mm/d at

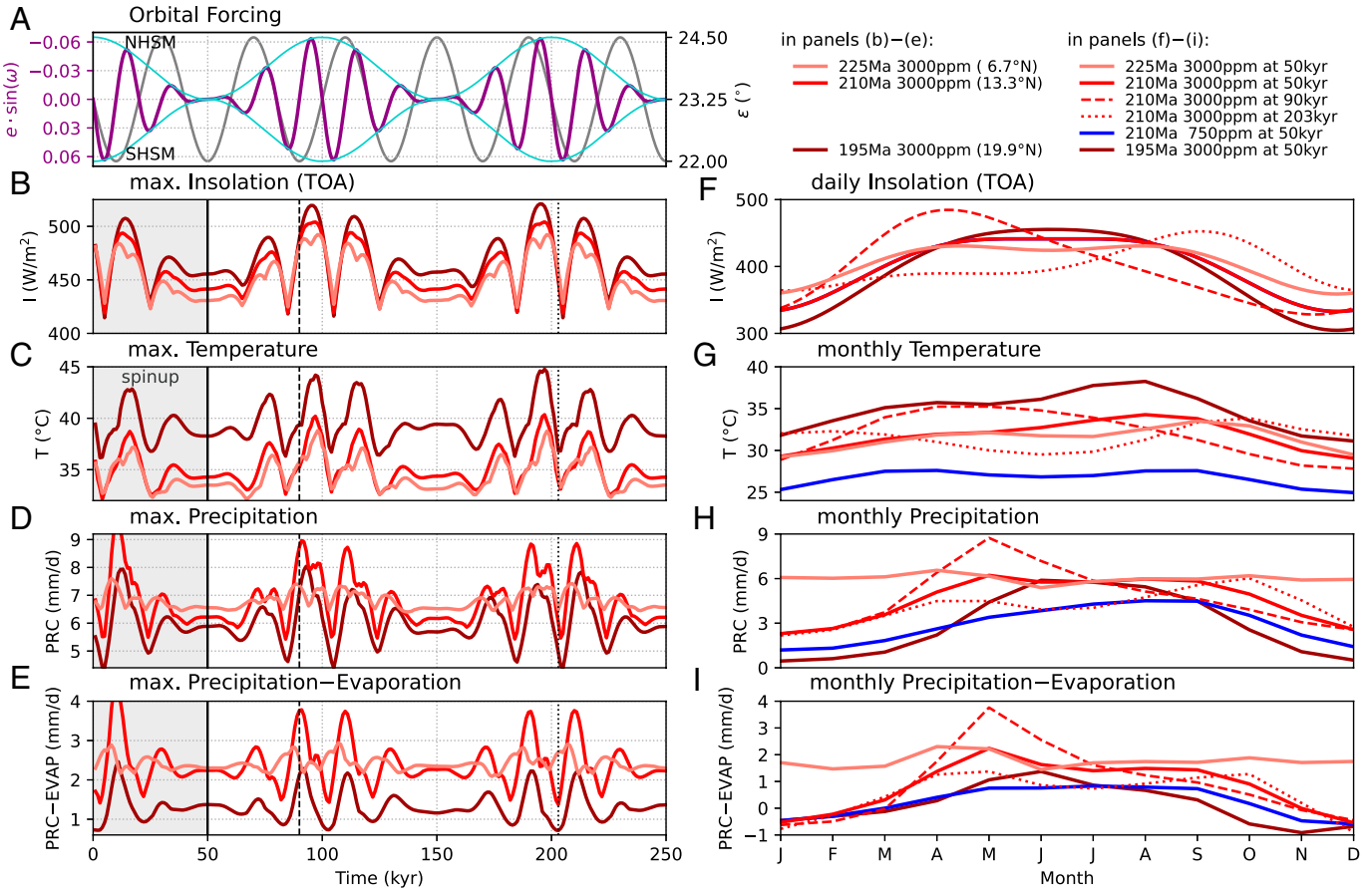

Fig. 2. Effect of the imposed orbital forcing on the regional climate conditions in the NHB area. (*A*) Orbital forcing expressed by the precession index $e \cdot \sin(\omega)$ (e, perihelion angle; ω, eccentricity) and obliquity ε. The left axis is inverted so that maximum Northern Hemisphere summer insolation (NHSM) occurs at the top. SHSM, maximum Southern Hemisphere summer insolation. (*B–E*) Maximum monthly values of regional climate quantities for three simulations at 225, 210, and 195 Ma (using $pCO_2 = 3{,}000$ ppm and the Geo_1 paleogeography). Vertical lines indicate three points in time for which monthly data are shown on the right side. (*F–I*) Monthly values of the same quantities at minimum ω and ε (at 50 ky; solid lines). Dashed and dotted lines for 210 Ma correspond to times of maximum and minimum PRC–EVAP, respectively, during a precession cycle at high ω and low ε (90 vs. 203 ky). Blue lines show low pCO_2 (750 ppm) for comparison with high pCO_2 (3,000 ppm) at 210 Ma.

220 Ma before falling to 1.8 to 2.8 mm/d at 195 Ma (also see *SI Appendix*, Fig. S3). The T seasonality (monthly maximum–minimum difference) rises from ∼6 to 8 °C, while the PRC seasonality grows from ∼2 mm/d to a peak of 5 to 6 mm/d at 200 Ma.

Because the NHB lake level cycles express changes in the hydrologic balance, the most relevant climatic parameter is the precipitation–evaporation difference (PRC–EVAP, or net precipitation). Following the modeled PRC^{ann}_{NHB} and T^{ann}_{NHB} trends, the most humid annual mean conditions occur around 220 Ma (*Net Precipitation Trends, Modulation, and Threshold Explain Lake Level Changes*), while potential evaporation exceeds precipitation after ∼200 Ma ($PRC–EVAP^{ann}_{NHB} \approx 0$; *SI Appendix*, Fig. S3), again showing the transition from humid to arid climate. The PRC–EVAP seasonality is highest during the intermediate 220 to 200 Ma period and reaches 3 mm/d, especially at high pCO_2. This increase under globally warmer climates is a general observation for T, PRC, PRC–EVAP, and their respective seasonality in the NHB area (*SI Appendix*, Fig. S3). The amplified seasonality is partly due to a strengthened late spring rainy season, as shown below, which is also relevant for the regional orbital climate response.

Strong Humidity Response to Precession during 220 to 200 Ma at High pCO_2

The modeled climate response in the NHB area to the employed orbital forcing (Fig. 2*A*) and the resulting local insolation changes (Fig. 2*B*) are illustrated by changes in the maximum T, PRC, and PRC–EVAP (Fig. 2 *C–E*) and their monthly values at different phases of the orbital forcing (Fig. 2 *F–I*). This is done for three time slices (225, 210, and 195 Ma) which represent the changing orbital response at different stages of the latitudinal and climatic shift. Overall, the effect of eccentricity-modulated precession is most evident, and the most warm and humid conditions generally occur around local insolation maxima corresponding to minima of the precessional index (Fig. 2, *Left*).

At 225 Ma and only ∼6 °N, the twice yearly solar zenith passage yields two annual insolation maxima and weak wet late spring (April to May) and warm late summer (August to September) seasons (Fig. 2, *Right*). As previously suggested (24, 25), the successive amplification of these two seasons shows up as double-precession peaks in the maximum insolation and PRC rates, but due to the weak seasonality, the precession effects are smaller than at later time slices and higher latitudes (Fig. 2, *Left*). Instead, the direct contribution of eccentricity to warmer and wetter conditions is more pronounced (see also *SI Appendix*, Fig. S3).

At 210 Ma and ∼13 °N, the secondary peaks remain visible due to the still broad summer and winter insolation plateaus. Nevertheless, the response to precession is much enhanced (Fig. 2, *Left*), especially at high pCO_2 values. The latter contribute to increased late spring rainfall (Fig. 2*G*), related to enhanced moisture transport and convergence from the Tethys reaching the NHB area (*SI Appendix*, Fig. S7). In contrast, maximum temperatures

and therefore evaporation occur in late summer (Fig. 2*G*) and are thus maximized later in the precession cycle (Fig. 2*C*). The late spring rainfall amplification early in the precession cycle (Fig. 2 *D* and *H*) is therefore not compensated by increased evaporation and leads to a strong $\mathrm{PRC–EVAP}^{\mathrm{max}}_{\mathrm{NHB}}$ response to precession (Fig. 2 *E* and *I*). This is also expressed by the relative lead of the $\mathrm{PRC}^{\mathrm{max}}_{\mathrm{NHB}}$ and $\mathrm{PRC–EVAP}^{\mathrm{max}}_{\mathrm{NHB}}$ response to the precession index (which peaks at maximum June insolation), whereas the temperature response lags behind (Fig. 2, *Left*). Similar relationships were reported by Marzocchi et al. (26) in the North African monsoon regions, which might be the closest modern analog for this NHB climate setting. Another analogy is a feedback by which heating is limited by increased rainfall and cloud coverage, amplifying humid periods in the seasonal and orbital cycles (*SI Appendix*, Fig. S6 and refs. 26–28). Previous work has indeed characterized Pangean climates by the dominant influence of large-scale monsoon patterns (29–35) and their astronomical modulation (e.g., refs. 12, 36, 37). These megamonsoon phenomena can be assessed with our modeling approach and provide context to the discussed climatic phenomena (*SI Appendix*, section 6) and will be addressed in further dedicated research.

By 195 Ma and ∼20 °N, more pronounced summer and winter seasons were established (Fig. 2, *Right*), so that peaks in the response occur closer to precession minima (Fig. 2, *Left*). The amplitudes of the $\mathrm{T}^{\mathrm{max}}_{\mathrm{NHB}}$ and $\mathrm{PRC}^{\mathrm{max}}_{\mathrm{NHB}}$ precession response are slightly larger than at 210 Ma due to the enhanced seasonality (Fig. 2 and *SI Appendix*, Fig. S1). However, the seasonality and orbital response of $\mathrm{PRC–EVAP}^{\mathrm{max}}_{\mathrm{NHB}}$ is actually reduced because the more closely coinciding maximum temperature and rainfall seasons compensate each other to a larger degree (Fig. 2).

To summarize, substantial precession-eccentricity effects on the low-latitude NHB regional climate are observed in the model results, with maximum rainfall and temperatures around the April to June and July to September maximum insolation phases of the precession cycle, respectively. The cyclic changes can exceed 7 °C, 3 mm/d, and 2 mm/d for maximum T, PRC, and PRC–EVAP (Fig. 2, *Left*). For PRC–EVAP, which represents the most direct link to reconstructed lake level cycles, they are most pronounced during the transitional phase from 220 to 200 Ma at high $p\mathrm{CO}_2$ (see also *SI Appendix*, Fig. S3). In earlier and later time slices they are limited by weak seasonality and increasing aridity, respectively.

Net Precipitation Trends, Modulation, and Threshold Explain Lake Level Changes

Now that we have established the context of simulated long-term climate trends (*Humid–Seasonal–Dry Climate Transition due to Continental Drift*) and orbital response (*Strong Humidity Response to Precession during 220 to 200 Ma at High* $p\mathrm{CO}_2$), physical links between the geologic record and modeled changes can be examined. Fig. 3 *A–G* summarizes relevant NHB proxy data, including lake depth levels derived from sediment color and facies (5–7), as well as amplitudes of precession- and eccentricity-scale periodicity in these time series (Fig. 3 *A–E*). Proxy data for $p\mathrm{CO}_2$ from the same strata suggest high levels until the early Rhaetian and around the Triassic–Jurassic boundary but lower values during the Rhaetian–Hettangian and around ∼211 Ma (38–40).

Fig. 3 *H–L* shows our climate model results for comparison. The simulations with high, medium, and low $p\mathrm{CO}_2$ are plotted or highlighted accordingly for each time slice (Fig. 3 *I–L*). Together they indicate a pathway of NHB mean climate and cyclicity, driven by orbital forcing, continental drift, and $p\mathrm{CO}_2$ changes. For this, we mainly consider PRC–EVAP and especially its monthly maximum values above a certain threshold (Fig. 3*I*) because it has been proposed that lake sediments from the NHB and also the Quaternary North African monsoon region actually record a truncated (or clipped, rectified) orbital climate signal in the hydrological balance (e.g., refs. 4, 24, 41–43). The reasoning is that lacustrine sediments record orbital changes when the lakes are filled by sufficient summer maximum rainfall at times of higher humidity, whereas they lack obvious sediment facies responses when lakes dry out during other orbital phases (ref. 42, chap. 9). Following this concept, the clipped $\mathrm{PRC–EVAP}^{\mathrm{max}}_{\mathrm{NHB}}$ (regional monthly maximum values; Fig. 3*I*) and their cyclicity (Fig. 3 *J* and *K*) show a remarkable consistency with the lake depth proxy record (Fig. 3 *B–E*) when a threshold value of 1.3 mm/d is assumed (Fig. 3*I*). This link between orbitally paced climate and lake level changes needs to be evaluated and extended in further work, perhaps with an explicit representation of basin hydrology.

The simulated NHB climate during 230 to 225 Ma is generally tropical humid, and the annual mean and maximum PRC–EVAP remain consistently above the threshold (Fig. 3*I*) at the high $p\mathrm{CO}_2$ levels suggested by the proxy record (Fig. 3*F*). The seasonality and the orbital response are small (Fig. 3 *I–L*). This fits to the persistent intermediate depth levels (Fig. 3*B*) and the low degree of cyclicity (Fig. 3*D*) expressed by the record in the Stockton Formation. However, all but the upper quarter of this formation is fluvial rather than lacustrine and is therefore less revealing in terms of high-frequency lacustrine cyclicity.

Toward 220 Ma, the mean and maximum PRC–EVAP strongly increase and reach their highest levels across all considered time slices (Fig. 3*I*). The seasonality and the precession-eccentricity response also show a marked increase (Fig. 3 *I–K*). This could partially explain the upward increase of cyclicity in lacustrine sediments in the upper Stockton Formation and the greatest prevalence of high water depths in the Lockatong Formation (5). However, this transition may also reflect a change in the balance between subsidence and accumulation rate (e.g., refs. 44, 45). Disentangling climate and sedimentary basin dynamics remains a challenge that needs to be addressed by future work.

Proceeding to 215 Ma, the seasonality and orbital response increased further, while the mean and maximum PRC–EVAP decreased (Fig. 3 *I–K*). This trend to somewhat drier but more variable conditions matches the lower minimum water depths and strong cyclicity found in the lower Passaic Formation (Fig. 3 *B–E*). This trend continues at 210 Ma in both the model and the record, where Olsen and Kent (5) noted a decreasing frequency of deep lake deposits and more frequent red beds (indicative of aridity) through the Passaic Formation. Within the transition from tropical humid to more seasonally arid climate classes, the orbital forcing is also recognized in temporary shifts between, e.g., *Af*, *Am*, and *Aw* climates (*SI Appendix*, Fig. S10*E*).

Around the Rhaetian 205 Ma time slice, proxy $p\mathrm{CO}_2$ values are consistently lower (Fig. 3*F*), and the PRC–EVAP clipping becomes important: in addition to the general aridification, $\mathrm{PRC–EVAP}^{\mathrm{max}}_{\mathrm{NHB}}$ is significantly reduced in a cooler climate at $p\mathrm{CO}_2 = 1{,}500$ ppm so that it only exceeds the threshold occasionally and then only slightly at maximum eccentricity and minimum precession (Fig. 3*I*). Consequently, the precessional orbital signal in the clipped $\mathrm{PRC–EVAP}^{\mathrm{max}}_{\mathrm{NHB}}$ time series is significantly reduced (Fig. 3 *I–K*), despite a strong orbital climate modulation that is, however, reduced by the lower $p\mathrm{CO}_2$ (*Strong Humidity Response to Precession during 220 to 200 Ma at High* $p\mathrm{CO}_2$). This could explain why the upper Passaic Formation records no deep lakes and muted precessional cyclicity in general (Fig. 3 *B–E*).

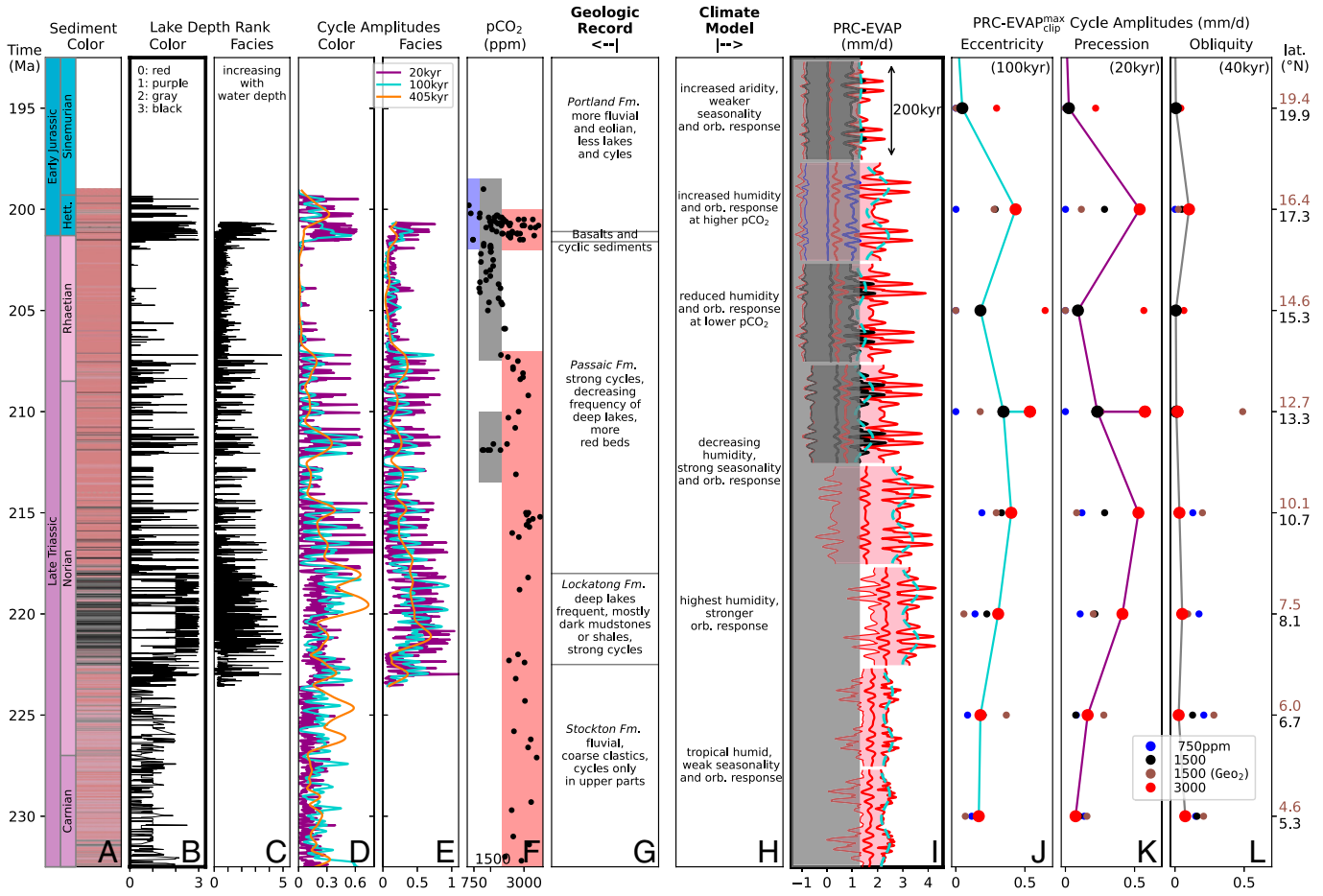

Fig. 3. Comparison of the NHB geologic lake level record (*A*–*G*) with simulated PRC–EVAP trends and orbital cyclicity (*H*–*L*). (*A*–*C*) Sediment color and lake depth levels from the composite record (6, 7). (*D* and *E*) Amplitudes of precession (∼20 ky) and eccentricity cycles (∼100 and ∼405 ky) in the depth levels (*B* and *C*), obtained from a continuous Morlet wavelet transform (*SI Appendix*, Fig. S10). (*F*) Proxy pCO_2 from Schaller et al. (38, 39) as reported by Foster et al. (40). Red, gray, and blue colors indicate intervals with relatively high, medium, and low values, respectively. (*G* and *H*) Notes regarding characteristics or upward trends inferred from proxy (5–7, 9, 11) or model data. (*I*) Simulated orbitally driven PRC–EVAP in the NHB area. For each time slice, maximum, mean, and minimum values are plotted for a transient 200-ky simulation at $pCO_2 = 3{,}000$ ppm (red) and additionally 1,500 or 750 ppm (black or blue) where lower pCO_2 values are suggested by proxy data (*F*). Turquoise lines indicate the eccentricity component, composed of the direct 100-ky signal and the amplitude modulation of the 20-ky precession cycle. The gray area indicates values below the assumed humidity threshold required for persistent lakes. The truncated/clipped $\text{PRC–EVAP}^{\text{max}}_{\text{NHB}}$ time series above this threshold are the potentially closest model analog to the depth levels in *B* and *C*. (*J*–*L*) Amplitudes of orbital signals in the clipped $\text{PRC–EVAP}^{\text{max}}_{\text{NHB}}$ time series in *I*, obtained with a Fourier transform. Compare with *D* and *E*. The eccentricity amplitude (*J*) accounts for both the 100-ky component and the modulation of precession (turquoise lines in *I*). Each dot represents one transient simulation, and bigger/connected dots indicate those which best reflect the proxy pCO_2 changes (*F*).

In contrast, recorded depth levels and cyclicity are clearly enhanced in the brief interval around the Triassic–Jurassic boundary (∼201.3 Ma), associated with the emplacement of the massive Central Atlantic Magmatic Province (CAMP) volcanism, also tied to the end-Triassic mass extinction (46–48). The climate simulations show that this is at least partly explained by the high pCO_2 levels recorded at this time because these lift $\text{PRC–EVAP}^{\text{max}}_{\text{NHB}}$ above the threshold so that a stronger cyclic climate modulation could be recorded under the more humid conditions (Fig. 3 *I*–*K*) (49).

Above the Triassic–Jurassic boundary, the PRC–EVAP seasonality and orbital modulation are reduced in the increasingly dry climate. Additionally, the humidity threshold is barely transgressed at the lower pCO_2 values suggested by the few pCO_2 data points. This trend is consistent with the observed increase in eolian strata above the lacustrine part of the Portland Formation (7). As already noted, both climatic and tectonic processes have influenced sediment deposition in the NHB (5). The replacement of lacustrine by fluvial strata in the upper Portland Formation may be due to a reduction of subsidence relative to the sediment supply rather than climate alone.

Low-Latitude Obliquity Signal from Shifting Tropical Rain Belt

Orbital climate cycles in the NHB area are generally dominated by precession and eccentricity (*Strong Humidity Response to Precession during 220 to 200 Ma at High pCO_2*). Evidence for obliquity effects had long been scarce (6), as expected from its minimal low-latitude radiative forcing, but was finally detected by recent work (49–51). This is supported here by a small but consistent obliquity signal in the simulated $\text{PRC–EVAP}^{\text{max}}_{\text{NHB}}$ time series, especially during 230 to 210 Ma (Fig. 3*L* and *SI Appendix*, Fig. S3).

This phenomenon is related to a stronger thermal contrast between the summer and winter hemispheres at high obliquity, which amplifies the seasonal shift of the Intertropical Convergence Zone (ITCZ) (*SI Appendix*, Fig. S9). The stronger northward shift of tropical rainfall during boreal summer supplies additional moisture to the NHB, especially during July to August (*SI Appendix*, Figs. S8 and S9). This is analogous to the obliquity effects on the North African monsoon (27, 28), including feedbacks that actually reduce summer temperatures and increase humidity, as also discussed for the response to precession

(*Strong Humidity Response to Precession during 220 to 200 Ma at High pCO_2*).

The obliquity signal in $PRC–EVAP^{max}_{NHB}$ is stronger at low pCO_2 (Fig. 3*L*) because at high pCO_2 the most humid season occurs in late spring (*Strong Humidity Response to Precession during 220 to 200 Ma at High pCO_2*) and is thus less modulated by the late summer maximum ITCZ deflection (*SI Appendix*, Fig. S8). The regional obliquity signal is also stronger for the Geo_2 paleogeographies (Fig. 3*L*), potentially related to the globally larger extent of land masses (*SI Appendix*, Fig. S1) and the farther inland position of the NHB. However, the basic effect is consistent across all simulations (*SI Appendix*, Fig. S9*B*). In fact, the observed obliquity signal appears nearly as strong as that of precession in the upper Passaic Formation (51), the interval with the lowest pCO_2.

To conclude, all three orbital parameters can increase NHB maximum humidity through elevated Northern Hemisphere insolation. The Carnian–Norian low-latitude obliquity signal reflects the response of the global circulation and the low-latitude hydrological regime to a high-latitude radiative forcing. As the NHB shifts northward, this indirect effect decays, but the direct insolation forcing appears in the regional temperatures (Fig. 3*L* and *SI Appendix*, Fig. S3). In contrast, precession and eccentricity yield a local radiative forcing without interhemispheric asymmetry that rather enhances the land–sea thermal contrast and moisture import from the Tethys (*SI Appendix*, Fig. S6).

Patterns of Orbital Climate Response Revealed by Other Proxy Localities

Our modeling approach can provide a global framework in which significant Late Triassic records mutually support the interpretation particularly of the differential climatic expression of astronomical pacing and paleogeographic shifts. Sophisticated analyses of these records are beyond the scope of this paper, but some insights suggest directions for future work.

For example, similar concepts for cyclic lake sediment deposition have been invoked for the Upper Triassic of the Germanic Basin (43, 52). In our model, this area receives significant summer rainfall from the Tethys (Fig. 1), and eccentricity-modulated precession dominates the T and PRC seasonality response around 225 Ma, with maxima at insolation peaks (also see *SI Appendix*, Figs. S11–S14). The modeled obliquity signal is very small but increases with the northward drift, which could explain its occurrence in younger parts of the basin (43).

A strong obliquity-scale pacing was inferred from fluvial–lacustrine sequences in the high-latitude Junggar Basin (∼200 Ma, ∼70 °N) (6, 53). A similarly strong response to obliquity and precession in the simulated T and PRC–EVAP supports this interpretation (see also *SI Appendix*, Figs. S15–S18). In contrast to the discussed lower-latitude localities, enhanced local insolation leads to drier conditions, and the PRC orbital response remains relatively small, suggesting a greater role of T and EVAP variations for the hydrological balance and cyclic lake sedimentation.

Proxy data from the Colorado Plateau (34, 54) suggest an aridification through the Late Triassic (55). The simulated regional conditions do indeed shift from tropical humid to desert climate between 220 and 205 Ma, with PRC^{ann} decreasing from 1,235 to 640 mm/y, while temperature averages and seasonality increase (also see *SI Appendix*, Figs. S19–S22). The small northward shift (∼4°) is apparently sufficient to leave the narrow tropical rain belt of western Pangea (Fig. 1 and *SI Appendix*, Fig. S19). While proxy cyclicality is being assessed (56), the simulations for the relevant time slices suggest that obliquity dominates the PRC and PRC–EVAP response through the discussed effect on ITCZ migration (*Low-Latitude Obliquity Signal from Shifting Tropical Rain Belt*). In contrast, the T response is dominated by eccentricity and an increasing precession component due to the northward drift, similar to the Newark Basin. This is a testable prediction for cores with climate proxy data and geochronology available for that area and time slice.

Conclusions

The climate model results presented here show that major features of the lake level record of the NHB can be understood through the combined climatic effects of orbital forcing, paleogeographic changes (especially the northward drift of Pangea), and atmospheric pCO_2 variations.

Tropical humid conditions with weak seasonality and orbital response prevail in the NHB area during the 230 to 225 Ma time slices (∼5 to 7 °N). Around 220 Ma (∼8 °N), a humidity maximum is reached and the orbital signal increases, coinciding with the deepest and consistently cyclical lake levels. From 215 to 205 Ma (∼10 to 15 °N), a shift from humid to drier and more seasonal monsoon and savanna climates matches the trend to less frequent deep-water lake deposits and more frequent aridity-related red beds. Although orbital climate modulation is high during the Rhaetian (∼205 Ma), the record exhibits low lake levels and low cyclicity. We show that this could be the result of a cooler, drier climate due to low pCO_2 and a threshold characteristic of lake filling and sedimentation. Proximal to the Triassic–Jurassic boundary (∼200 Ma, ∼17 °N), volcanic emissions from the Central Atlantic Magmatic Province (CAMP) temporarily elevated pCO_2 levels, contributing once again to enhanced humidity and cyclicity in the model, supporting empirical findings. After 195 Ma (⩾20 °N), semiarid climates with reduced seasonality and orbital response are established and intensified by lower pCO_2. This is mirrored by the onset of muted lake level variability and possibly replacement by fluvial and eolian environments.

Our simulations extend evidence for a strong response of tropical Pangean climates to astronomical forcings, despite or even because of a warm and ice-free greenhouse world. Despite the primary role of precession and eccentricity, obliquity is found to affect low-latitude hydrological regimes by modulating the seasonal shift of the tropical rainfall belt.

Extending this global model framework and these data to other contemporaneous records yields a more complete picture of Late Triassic climate trends and orbital forcing. For example, in both the Colorado Plateau and Junggar Basin, humidity regimes appear more prone to obliquity than in the NHB because of either ITCZ rainfall (Colorado Plateau) or high-latitude radiative forcing (Junggar Basin).

The fast CLIMBER-X Earth System Model (19) utilized here provides enhanced opportunities for future studies on astronomical climate dynamics in various paleoclimatic contexts that could address the role of carbon cycle and ice sheet feedbacks as well as the orbital pacing of global sea level oscillations. Regarding the latter, contributions of aquifer eustasy (57–60) and glacioeustatic effects in greenhouse climate states await clarification. Further work would complement recent research that suggests an antiphased relation between changes in continental water storage indicated by the NHB lake level record and Late Triassic global sea level cycles, supporting an astronomical modulation of groundwater recharge and discharge as the common driver (50, 61). The secular NHB lake level shallowing trend obtained from sedimentary noise modeling above the Stockton Formation (61) agrees with

the simulated PRC–EVAP decrease (Fig. 3*I*; see also *SI Appendix*, Fig. S5).

Materials and Methods

Model Description. All simulations were conducted with CLIMBER-X (19), which is a comprehensive Earth system model of intermediate complexity, designed to simulate the evolution of the Earth system on decadal to orbital time scales. In this study, the coupled statistical–dynamical atmosphere (SESAM) (19), three-dimensional frictional–geostrophic ocean (GOLDSTEIN) (62), dynamic–thermodynamic sea ice (SISIM) (19), and land surface and vegetation modules (PALADYN) (63) are used and run on a 5° × 5° horizontal grid. Predecessors of the model have been applied to study orbital climate dynamics in the Neogene and Quaternary, for example, regarding glacial cycles (64) or the African monsoon (65). Within the large ranges spanned by different models and uncertain boundary conditions, the general climate patterns obtained from the CLIMBER-X compare reasonably with other published results (*SI Appendix*, section 8).

Boundary Conditions. An ensemble of 36 climate simulations was performed, representing a set of nine geological time slices from 230 to 190 Ma in 5-My steps with paleogeographies based on reconstructions by Marcilly et al. (20) ($\mathtt{Geo}_1$) and Cao et al. (21) ($\mathtt{Geo}_2$). Both distinguish qualitatively between exposed land, shallow marine, and deep marine areas, and Cao et al. (21) additionally represent major mountain ranges (*SI Appendix*, section 1 for further information). Unless otherwise indicated, we refer to the simulations with $\mathtt{Geo}_1$, which serves as a generalized basis for the majority of simulations. To abstract from the influence of uncertain local topography changes and enable comparability between the geological time slices, the NHB neighborhood is always set to lowland elevation. Due to the limited spatial accuracy of global Earth system models and available global paleogeographic models, local topographic dynamics of the NHB and its catchment area are not represented more comprehensively here. Nevertheless, these changes could have important effects on the local climate and hydrology. Air temperatures generally decrease with elevation, and the terrain modulates precipitation by influencing wind and moisture transport patterns. Topography also dictates the routing of water in the basin catchment, and basin subsidence together with sediment supply must have affected lake depths and the sedimentary environment. Furthermore, water could have been extracted by riverine discharge, in addition to evaporation. This study uses the simplifying assumption that the regional hydrological regime was, nevertheless, primarily set by precipitation and evaporation, dictated by large-scale climatic patterns. Further research could aim to add a more detailed representation of the basin topography and hydrology to this global-scale climate modeling.

Simulations were conducted for atmospheric CO_2 concentrations fixed at 750, 1,500, or 3,000 ppm with $\mathtt{Geo}_1$ and 1,500 ppm with $\mathtt{Geo}_2$. This is to assess differences between overall warmer and cooler climate states, considering the temporal variation and uncertainty of pCO_2 reconstructions for that time period as compiled by Foster et al. (40), which includes measurements on paleosol carbonates from the NHB (66) (Fig. 3*F*). The solar constant was set according to standard solar evolution (67) relative to its present-day value of 1,361 W/m^2 (68) and increases from 1,335.4 W/m^2 at 230 Ma to 1,339.8 W/m^2 at 190 Ma.

Forcings. The simulations were run for 250,000 model years and exposed to an orbital forcing that cyclically modulates the orbital parameters eccentricity (e), longitude of the perihelion (precession angle ω), and obliquity (axial tilt ε; Fig. 2*A*). As the purpose of this study is to investigate general effects of these parameters rather than to evaluate specific astronomical solutions, the idealized forcing contains only three periodicities (similar to ref. 15): 100, 40, and 20 ky representing the ∼100-ky short orbital eccentricity cycle, the 41-ky obliquity cycle, and the 19- to 23-ky climatic precession band in today's solar system.

Running and Analyzing the Model Simulations. The fastest external change in the simulations is the precession cycle that acts on an ∼10-ky time scale. This exceeds the general response time of surface climate conditions that are analyzed here and allows a climate model iteration for updated boundary conditions to be run every 5 y, ideally resulting in a 5× model acceleration. This is similar to approaches achieving transient climate simulations on 100-ky time scales for the Quaternary (69–71). Only the final 200 ky of the simulations were used here for analyses, while the first 50 ky are considered as a spin-up period (effectively corresponding to 10,000 model years, considering the 5× acceleration). In the stratigraphic terminology of the NHB record, the simulated time series each reflect 10 Van Houten and 2 short modulating cycles each (9). Although the model provides global climate information, this study focuses particularly on regional conditions relevant for the deposition of the NHB sediment record. Therefore, model output was averaged over a radius of 600 km around the reconstructed central location (*SI Appendix*, Table S1), which is indicated by circles in all of the maps (e.g., Fig. 1). This corresponds to the approximate equatorial model grid cell size and also reflects the extent of the basins catchment area as well as uncertain paleogeographic and depositional settings which all prevent a more confined local assessment.

Data, Materials, and Software Availability. Model input and output files for all simulations as well as the scripts to generate the figures are available at the institutional repository of the Potsdam Institute for Climate Impact Research (PIK) (72) (https://dx.doi.org/10.5880/PIK.2022.001/). The repository also includes the utilized model source code which was obtained on 8 October 2021, commit e7b58adad8c798ef5c5e28c3b6d398a19c36f78a in PIK's institutional gitlab repository. The CLIMBER-X model is described by Willeit et al. (19), and version 1.0 is provided at https://doi.org/10.5281/zenodo.6877358 (73), which is an update of the code used for these simulations.

ACKNOWLEDGMENTS. We thank C. M. Marcilly, W. Cao, and colleagues for making their paleogeographic models available. The European Regional Development Fund, the German Federal Ministry of Education and Research, and the Land Brandenburg are gratefully acknowledged for supporting this project by providing resources on the high-performance computer system at the Potsdam Institute for Climate Impact Research. M. Wagreich and B.S. acknowledge support by the Austrian Academy of Sciences (ÖAW), International Programs, Earth System Sciences (ESS), in the frame of "United Nations Educational, Scientific and Cultural Organization/International Union of Geosciences (UNESCO/IUGS)," International Geoscience Programme projects 661, and IGCP 710, respectively. M. Willeit acknowledges support by the project PalMod, funded by the German Federal Ministry of Education and Research. We thank two anonymous reviewers for their constructive feedback.

Author affiliations: [a]Department of Geology, University of Vienna, 1090 Vienna, Austria; [b]Earth System Analysis, Potsdam Institute for Climate Impact Research, Member of the Leibniz Association, D-14412 Potsdam, Germany; [c]Ocean and Earth Science, National Oceanography Centre, University of Southampton, SO14 3ZH Southampton, United Kingdom; [d]Department of Geological Sciences, San Diego State University, San Diego, CA 92182; and [e]Biology and Paleo Environment Division, Lamont-Doherty Earth Observatory of Columbia University, Palisades, 10968 NY

1. M. Milankovitch, Kanon der Erdbestrahlung und seine Anwendung auf das Eiszeitenproblem. *R. Serbian Acad. Spec. Publ.* **133**, 1–633 (1941).
2. J. D. Hays, J. Imbrie, N. J. Shackleton, Variations in the Earth's orbit: Pacemaker of the ice ages. *Science* **194**, 1121–1132 (1976).
3. A. Berger, Q. Yin, "Astronomical theory and orbital forcing" in *The SAGE Handbook of Environmental Change*, J. Matthews, Ed. (SAGE Publications Ltd, 2012), vol. 1, pp. 405–425.
4. L. A. Hinnov, "Cyclostratigraphy and astrochronology in 2018" in *Cyclostratigraphy and Astrochronology, Stratigraphy & Timescales*, M. Montenari, Ed. (Academic Press, 2018), vol. 3, pp. 1–80.
5. P. E. Olsen, D. V. Kent, Milankovitch climate forcing in the tropics of Pangaea during the Late Triassic. *Palaeogeogr. Palaeoclimatol. Palaeoecol.* **122**, 1–26 (1996).
6. P. E. Olsen *et al.*, Mapping Solar System chaos with the Geological Orrery. *Proc. Natl. Acad. Sci. U.S.A.* **116**, 10664–10673 (2019).
7. D. V. Kent, P. E. Olsen, G. Muttoni, Astrochronostratigraphic polarity time scale (APTS) for the Late Triassic and Early Jurassic from continental sediments and correlation with standard marine stages. *Earth Sci. Rev.* **166**, 153–180 (2017).
8. P. E. Olsen, A 40-million-year lake record of early Mesozoic orbital climatic forcing. *Science* **234**, 842–848 (1986).
9. P. E. Olsen, D. V. Kent, B. Cornet, W. K. Witte, R. W. Schlische, High-resolution stratigraphy of the Newark rift basin (early Mesozoic, eastern North America). *Bull. Geol. Soc. Am.* **108**, 40–77 (1996b).
10. P. E. Olsen, D. V. Kent, Continental coring of the Newark Rift. *Eos* **71**, 385–394 (1990).
11. P. E. Olsen, D. V. Kent, Long-period Milankovitch cycles from the Late Triassic and Early Jurassic of eastern North America and their implications for the calibration of the Early Mesozoic time-scale and the long-term behaviour of the planets. *Philos. Trans. R. Soc. London. Ser. A Math. Phys. Eng. Sci.* **357**, 1761–1786 (1999).

12. J. E. Kutzbach, "Idealized Pangean climates - Sensitivity to orbital change" in *Pangea: Paleoclimate, Tectonics, and Sedimentation during Accretion, Zenith and Breakup of a Supercontinent*, G. D. Klein, Ed. (Spec. Pap. 288, Geological Society of America, 1994), pp. 41–55.
13. P. J. Valdes, B. W. Sellwood, G. D. Price, Modelling Late Jurassic Milankovitch climate variations. *Geol. Soc. Lond. Spec. Publ.* **85**, 115–132 (1995).
14. D. E. Horton, C. J. Poulsen, D. Pollard, Influence of high-latitude vegetation feedbacks on late Palaeozoic glacial cycles. *Nat. Geosci.* **3**, 572–577 (2010).
15. D. E. Horton, C. J. Poulsen, I. P. Montañez, W. A. DiMichele, Eccentricity-paced late Paleozoic climate change. *Palaeogeogr. Palaeoclimatol. Palaeoecol.* **331-332**, 150–161 (2012).
16. G. Feulner, Formation of most of our coal brought Earth close to global glaciation. *Proc. Natl. Acad. Sci. U.S.A.* **114**, 11333–11337 (2017).
17. J. Brugger, M. Hofmann, S. Petri, G. Feulner, On the sensitivity of the Devonian climate to continental configuration, vegetation cover, orbital configuration, CO_2 concentration, and insolation. *Paleoceanogr. Paleoclimatol.* **34**, 1375–1398 (2019).
18. J. Landwehrs, G. Feulner, S. Petri, B. Sames, M. Wagreich, Investigating Mesozoic climate trends and sensitivities with a large ensemble of climate model simulations. *Paleoceanogr. Paleoclimatol.* **36**, e2020PA004134 (2021).
19. M. Willeit, A. Ganopolski, A. Robinson, N. R. Edwards, The Earth system model CLIMBER-X v1.0–Part 1: Climate model description and validation. *Geosci. Model Dev.* **15**, 5905–5948 (2022).
20. C. M. Marcilly, T. H. Torsvik, M. Domeier, D. L. Royer, New paleogeographic and degassing parameters for long-term carbon cycle models. *Gondwana Res.* **97**, 176–203 (2021).
21. W. Cao *et al.*, Improving global paleogeography since the late Paleozoic using paleobiology. *Biogeosciences* **14**, 5425–5439 (2017).
22. W. Cao *et al.*, Palaeolatitudinal distribution of lithologic indicators of climate in a palaeogeographic framework. *Geol. Mag.* **156**, 331–354 (2018).
23. H. E. Beck *et al.*, Present and future Köppen-Geiger climate classification maps at 1-km resolution. *Sci. Data* **5**, 180214 (2018).
24. T. J. Crowley, K. Y. Kim, J. G. Mengel, D. A. Short, Modeling 100,000-year climate fluctuations in pre-Pleistocene time series. *Science* **255**, 705–707 (1992).
25. J. H. Whiteside, D. S. Grogan, P. E. Olsen, D. V. Kent, Climatically driven biogeographic provinces of Late Triassic tropical Pangea. *Proc. Natl. Acad. Sci. U.S.A.* **108**, 8972–8977 (2011).
26. A. Marzocchi *et al.*, Orbital control on late Miocene climate and the North African monsoon: Insight from an ensemble of sub-precessional simulations. *Clim. Past* **11**, 1271–1295 (2015).
27. J. H. C. Bosmans, S. S. Drijfhout, E. Tuenter, F. J. Hilgen, L. J. Lourens, Response of the North African summer monsoon to precession and obliquity forcings in the EC-Earth GCM. *Clim. Dyn.* **44**, 279–297 (2015).
28. J. H. C. Bosmans, F. J. Hilgen, E. Tuenter, L. J. Lourens, Obliquity forcing of low-latitude climate. *Clim. Past* **11**, 1335–1346 (2015).
29. J. Totman Parrish, A. Ziegler, C. R. Scotese, Rainfall patterns and the distribution of coals and evaporites in the Mesozoic and Cenozoic. *Palaeogeogr. Palaeoclimatol. Palaeoecol.* **40**, 67–101 (1982).
30. J. Totman Parrish, Climate of the supercontinent Pangea. *J. Geol.* **101**, 215–233 (1993).
31. J. E. Kutzbach, R. G. Gallimore, Pangaean climates: Megamonsoons of the megacontinent. *J. Geophys. Res.* **94**, 3341–3357 (1989).
32. R. F. Dubiel, J. T. Parrish, J. M. Parrish, S. C. Good, The Pangaean Megamonsoon: Evidence from the upper Triassic Chinle formation, Colorado Plateau. *Palaios* **6**, 347–370 (1991).
33. P. X. Wang *et al.*, The global monsoon across timescales: Coherent variability of regional monsoons. *Clim. Past* **10**, 2007–2052 (2014).
34. L. Nordt, S. Atchley, S. Dworkin, Collapse of the Late Triassic megamonsoon in western equatorial Pangea, present-day American Southwest. *Geol. Soc. Am. Bull.* **127**, 1798–1815 (2015).
35. C. A. Shields, J. T. Kiehl, Monsoonal precipitation in the Paleo-Tethys warm pool during the latest Permian. *Palaeogeogr. Palaeoclimatol. Palaeoecol.* **491**, 123–136 (2018).
36. A. Winguth, C. Winguth, Precession-driven monsoon variability at the Permian-Triassic boundary – Implications for anoxia and the mass extinction. *Global Planet. Change* **105**, 160–170 (2013).
37. M. Ikeda, K. Ozaki, J. Legrand, Impact of 10-Myr scale monsoon dynamics on Mesozoic climate and ecosystems. *Sci. Rep.* **10**, 11984 (2020).
38. M. F. Schaller, J. D. Wright, D. V. Kent, Atmospheric pCO_2 perturbations associated with the Central Atlantic Magmatic Province. *Science* **331**, 1404–1409 (2011).
39. M. F. Schaller, J. D. Wright, D. V. Kent, P. E. Olsen, Rapid emplacement of the Central Atlantic Magmatic Province as a net sink for CO_2. *Earth Planet. Sci. Lett.* **323-324**, 27–39 (2012).
40. G. L. Foster, D. L. Royer, D. J. Lunt, Future climate forcing potentially without precedent in the last 420 million years. *Nat. Commun.* **8**, 14845 (2017).
41. R. Y. Anderson, Enhanced climate variability in the tropics: A 200 000 yr annual record of monsoon variability from Pangea's equator. *Clim. Past* **7**, 757–770 (2011).
42. W. R. Ruddiman, *Earth's Climate: Past and Future* (W. H. Freeman and Company, ed. 3, 2014).
43. A. Bahr *et al.*, Mega-monsoon variability during the late Triassic: Re-assessing the role of orbital forcing in the deposition of playa sediments in the Germanic Basin. *Sedimentology* **67**, 951–970 (2020).
44. R. W. Schlische, P. E. Olsen, Quantitative filling model for continental extensional basins with applications to early Mesozoic rifts of Eastern North America. *J. Geol.* **98**, 135–155 (1990).
45. J. Contreras, C. H. Scholz, Evolution of stratigraphic sequences in multisegmented continental rift basins: Comparison of computer models with the basins of the East African rift system. *AAPG Bull.* **85**, 1565–1581 (2001).
46. A. Marzoli *et al.*, Extensive 200-million-year-Old continental flood basalts of the central Atlantic magmatic province. *Science* **284**, 616–618 (1999).
47. T. J. Blackburn *et al.*, Zircon U-Pb geochronology links the end-Triassic extinction with the Central Atlantic Magmatic Province. *Science* **340**, 941–945 (2013).
48. J. Landwehrs, G. Feulner, M. Hofmann, S. Petri, Climatic fluctuations modeled for carbon and sulfur emissions from end-Triassic volcanism. *Earth Planet. Sci. Lett.* **537**, 116174 (2020).
49. J. Whiteside, M. Schaller, P. Olsen, M. Margulis-Ohnuma, J. Yager, "An overture to the Anthropocene: Isotopic evidence of strong CO_2 modulation of the tropical monsoon at the dawn of dinosaurs" in *Conference Proceedings, 30th International Meeting on Org. Geochem. (IMOG 2021)* (European Association of Geoscientists & Engineers, 2021), pp. 1–2.
50. L. Hinnov, A. Cozzi, Rhaetian (Late Triassic) Milankovitch cycles in the Tethyan Dachstein limestone and Laurentian Passaic formation linked by the g2-g5 astronomical metronome. *Bol. Geol. Min.* **31**, 269–290 (2021).
51. M. Margulis-Ohnuma, J. Whiteside, P. Olsen, Strong inclination pacing of climate in Late Triassic low latitudes revealed by the Earth-Saturn tilt cycle. *Yale Undergrad. Res. J.* **2**, 37 (2021).
52. T. Vollmer *et al.*, Orbital control on Upper Triassic Playa cycles of the Steinmergel-Keuper (Norian): A new concept for ancient playa cycles. *Palaeogeogr. Palaeoclimatol. Palaeoecol.* **267**, 1–16 (2008).
53. J. Sha *et al.*, Triassic-Jurassic climate in continental high-latitude Asia was dominated by obliquity-paced variations (Junggar Basin, Ürümqi, China). *Proc. Natl. Acad. Sci. U.S.A.* **112**, 3624–3629 (2015).
54. R. F. Dubiel, S. T. Hasiotis, "Deposystems, paleosols, and climatic variability in a continental system: The upper Triassic Chinle formation, Colorado Plateau, U.S.A." in *From River to Rock Record: The Preservation of Fluvial Sediments and Their Subsequent Interpretation*, S. K. Davidson, S. Leleu, C. P. North, Eds. (SEPM Society for Sedimentary Geology, 2011), pp. 393–421.
55. C. J. Lepre, P. E. Olsen, Hematite reconstruction of Late Triassic hydroclimate over the Colorado Plateau. *Proc. Natl. Acad. Sci. U.S.A.* **118**, e2004343118 (2021).
56. C. Lepre, O. Yazzie, P. Olsen, "Orbital pacing of redox cycles suggested by red bed color of the Late Triassic Chinle Formation, Arizona" in *EGU General Assembly Conference Abstracts* (2021), pp. EGU21-3696.
57. M. Wagreich, R. Lein, B. Sames, Eustasy, its controlling factors, and the limno-eustatic hypothesis–Concepts inspired by Eduard Suess. *Aust. J. Earth Sci.* **107**, 115–131 (2014).
58. M. Li, L. A. Hinnov, C. Huang, J. G. Ogg, Sedimentary noise and sea levels linked to land-ocean water exchange and obliquity forcing. *Nat. Commun.* **9**, 1004 (2018).
59. B. Sames *et al.*, Review: Short-term sea-level changes in a greenhouse world–A view from the Cretaceous. *Palaeogeogr. Palaeoclimatol. Palaeoecol.* **441**, 393–411 (2016).
60. B. Sames, M. Wagreich, C. P. Conrad, S. Iqbal, Aquifer-eustasy as the main driver of short-term sea-level fluctuations during Cretaceous hothouse climate phases. *Geol. Soc. Lond. Spec. Publ.* **498**, 9–38 (2020).
61. M. Wang, M. Li, D. B. Kemp, S. Boulila, J. G. Ogg, Sedimentary noise modeling of lake-level change in the Late Triassic Newark Basin of North America. *Global Planet. Change* **208**, 103706 (2022).
62. N. R. Edwards, R. Marsh, Uncertainties due to transport-parameter sensitivity in an efficient 3-D ocean-climate model. *Clim. Dyn.* **24**, 415–433 (2005).
63. M. Willeit, A. Ganopolski, Paladyn v1.0, a comprehensive land surface–vegetation–carbon cycle model of intermediate complexity. *Geosci. Model Dev.* **9**, 3817–3857 (2016).
64. M. Willeit, A. Ganopolski, R. Calov, V. Brovkin, Mid-Pleistocene transition in glacial cycles explained by declining CO_2 and regolith removal. *Sci. Adv.* **5**, eaav7337 (2019).
65. B. de Boer, M. Peters, L. J. Lourens, The transient impact of the African monsoon on Plio-Pleistocene Mediterranean sediments. *Clim. Past* **17**, 331–344 (2021).
66. M. F. Schaller, J. D. Wright, D. V. Kent, A 30 Myr record of Late Triassic atmospheric pCO_2 variation reflects a fundamental control of the carbon cycle by changes in continental weathering. *Bull. Geol. Soc. Am.* **127**, 661–671 (2015).
67. J. N. Bahcall, M. H. Pinsonneault, S. Basu, Solar models: Current epoch and time dependences, neutrinos, and helioseismological properties. *Astrophys. J.* **555**, 990–1012 (2001).
68. G. Kopp, J. L. Lean, A new, lower value of total solar irradiance: Evidence and climate significance. *Geophys. Res. Lett.* **38**, 1–7 (2011).
69. J. E. Kutzbach, X. Liu, Z. Liu, G. Chen, Simulation of the evolutionary response of global summer monsoons to orbital forcing over the past 280,000 years. *Clim. Dyn.* **30**, 567–579 (2008).
70. J. E. Kutzbach *et al.*, African climate response to orbital and glacial forcing in 140,000-y simulation with implications for early modern human environments. *Proc. Natl. Acad. Sci. U.S.A.* **117**, 2255–2264 (2020).
71. M. Tigchelaar, A. Timmermann, D. Pollard, T. Friedrich, M. Heinemann, Local insolation changes enhance Antarctic interglacials: Insights from an 800,000-year ice sheet simulation with transient climate forcing. *Earth Planet. Sci. Lett.* **495**, 69–78 (2018).
72. J. Landwehrs *et al.*, Data from climate model simulations for Triassic–Jurassic orbital climate cycles. GFZ Data Services. https://dx.doi.org/10.5880/PIK.2022.001/. Deposited 19 October 2022.
73. M. Willeit, CLIMBER-X v1.0. Zenodo. https://doi.org/10.5281/zenodo.6877358. Deposited 27 February 2022.